



Study of Magnetic and Temperature-Dependent Dielectric Properties of Co-CuFe₂O₄ Nanoferrites

Reena Dhyani¹ · R. C. Srivastava¹ · Gagan Dixit¹

Received: 26 February 2022 / Accepted: 11 July 2022 / Published online: 4 August 2022
© The Minerals, Metals & Materials Society 2022

Abstract

The present study focuses on the investigation of magnetic and temperature-dependent dielectric properties of Co-CuFe₂O₄ nanoferrites. CuFe₂O₄, Cu_{0.5}Co_{0.5}Fe₂O₄ and CoFe₂O₄ nanoparticles were prepared using sol-gel auto-combustion. X-ray diffraction (XRD) pattern shows a phase transformation from tetragonal (for CuFe₂O₄) to cubic (for Cu_{0.5}Co_{0.5}Fe₂O₄ and CoFe₂O₄) structure. Surface morphology of synthesized samples was analyzed by scanning electron microscopy, which shows formation of agglomerated, irregular shaped nanoparticles. Fourier transform infrared and Raman spectra of CuFe₂O₄, Cu_{0.5}Co_{0.5}Fe₂O₄ and CoFe₂O₄ nanoparticles support the results of XRD analysis. The UV-visible spectra of all the samples show strong absorption maxima in the visible range and are used to calculate the energy band gap of the synthesized nanoferrites. It was noticed that the value of band gap is highest for CuFe₂O₄ (1.58 ± 0.02 eV) nanoparticles in comparison to Cu_{0.5}Co_{0.5}Fe₂O₄ (1.18 ± 0.02 eV) and CoFe₂O₄ (1.01 ± 0.02 eV) ferrite systems. Magnetic study shows the highest value of coercivity (H_c) and squareness ratio (S) for Cu_{0.5}Co_{0.5}Fe₂O₄ ($H_c = 959.10 \pm 0.30$ Oe, and $S = 0.45 \pm 0.05$) ferrite. The dielectric measurement revealed a significantly lower value of tangent loss ($\tan\delta$) at higher frequencies for Cu_{0.5}Co_{0.5}Fe₂O₄ and CoFe₂O₄ ferrite samples in comparison to that for CuFe₂O₄. The high value of magnetic parameters, high resistivity ($\sim 10^7$ – 10^8 Ω cm), and low dielectric loss at high frequencies for Cu_{0.5}Co_{0.5}Fe₂O₄ and CoFe₂O₄ nanoferrites suggests that the materials are potential candidate for high density magnetic recording media and also to be used in power transformers at high frequencies.

Keywords Nanoferrites · saturation magnetization · coercivity · dielectric constant

Introduction

Nanotechnology has initiated a renewed interest in the field of material's science to explore the properties of materials and enhance their technological applications in comparison to their bulk counterpart. Spinel ferrites are attractive multi-functional ferrimagnetic materials that have attracted much attention of researchers due to their outstanding magnetic, electrical, and optical properties.^{1–4}

Copper ferrite, with the chemical formula CuFe₂O₄, where Cu and Fe ions exist in divalent and trivalent states, respectively, is an important inverse spinel ferrite.

CuFe₂O₄ is known to crystallize in either tetragonal (I4I₁ and space group) or cubic (Fd3m space group) structure depending upon the annealing temperature.⁵ In copper ferrite, the tetragonal phase arises from distortion along one axis of the octahedron ($c/a > 1$), caused by the presence of Cu⁺² ions (d^9) in octahedral position. It was observed that in tetragonal phase, the copper ferrite is always partially inverted, and the inversion parameter depends on the synthesis condition, annealing temperature, and the cooling mode.⁶ The soft magnetic material CuFe₂O₄, has interesting properties due to its ferrimagnetic behavior, high resistivity, and low eddy current losses. Because of such fascinating properties, it provides a variety of promising scientific and technological applications in optoelectronic devices,⁷ catalyst,⁸ sensors,⁹ microwave devices,¹⁰ etc. On the other hand, CoFe₂O₄ is a well-known hard magnetic material which exhibits high coercivity along with a moderate saturation magnetization ~ 80 emu g⁻¹ and high Curie

✉ Reena Dhyani
reenadhyanil6@gmail.com

¹ Department of Physics, G. B. Pant University of Agriculture and Technology, Pantnagar 263145, India

temperature (672 ± 5 K).³ The value of room temperature resistivity for cobalt ferrite is about 1.44×10^8 Ωcm .³ The low value of dielectric loss at high frequencies with excellent magnetic properties makes it a promising candidate for microwave application as well as high-density storage devices.

It is crucial to focus on the study of the physical properties of materials to explore their innovative applications. The synthesis of nanostructured materials with controlled size, shape, and morphology is critical for scientific and technological applications. It was noticed that the properties of ferrite nanoparticles crucially depend on the method of synthesis, reaction time, annealing temperature, annealing time, distribution of cations at tetrahedral (*A*) and octahedral sites (*B*), introduction of dopants, etc.¹¹ Different synthesis techniques have their own limitations as well as benefits. Sol-gel auto-combustion is an economical method which produces homogenous ultrafine particles, with high purity and controllable size.¹² Several researchers have studied the structural and magnetic properties of Co-substituted ferrites, such as Ni-Zn ferrite,^{12,13} Li ferrite,¹⁴ Ba-Sr ferrite,¹⁵ Mn-Zn,¹⁶ Mg ferrite,¹⁷ and Ni ferrite.¹⁸ The substitution of cations at the *A* and *B* sites produces significant changes in the physical and chemical properties of parent ferrite nanoparticles.

The partial substitution of transition metals,^{12,13} rare earth elements in spinel ferrites¹⁹ and nanocomposites of ferrites/multiferroics,²⁰ ferrite/polymer,²¹ ferrite/grapheme oxide,²² ferrite/metal oxides,²³ etc. are at the forefront of modern research to modify the properties of ferrites. Recent studies confirmed that Co-substituted copper ferrite offers advantages as an excellent microwave absorber,²⁴ a photocatalyst,²⁵ high-performance supercapacitor, in biomedical application,²⁶ etc. However, only few reports are available that explain the properties of cobalt substituted copper ferrites. Bhaskaran et al.²⁷ examined the magnetic properties of Co_{1-x}Cu_xFe₂O₄ ($x = 0.0, 0.1, 0.2, 0.4, 0.6, 0.8$ and 1.0) nanoparticles. They observed that the crystal structure undergoes transformation from tetragonal to cubic with increasing concentration of Co⁺² ions. The saturation magnetization and coercivity was maximum for compositions $x = 0.8$ and $x = 1.0$, respectively. The magnetic anisotropy and remanent magnetization was found to increase with increasing content of Co⁺² ions. The dielectric properties of the Cu_{1-x}Co_xFe₂O₄ ($x = 0.0, 0.1, 0.2, 0.4, 0.6$ and 1.0) ferrite system was measured at room temperature in the frequency range of 1 kHz-1 MHz by Dar et al.²⁸ These nanoparticles were prepared by a solid-state reaction. The highest value of dielectric constant (ϵ) was found to be 4.2×10^5 for composition $x = 0.1$ and it starts to decrease with increasing Co concentration. Thus, more investigations are required, as different compositions show different behavior depending upon the method of synthesis. Therefore, in the present work, we study all electrical and magnetic properties of 50%

Co-substituted CuFe₂O₄ ferrites, to eliminate diverse effects arising from the method of synthesis and composition.

Experimental Section

To synthesize CuFe₂O₄, Cu_{0.5}Co_{0.5}Fe₂O₄ and CoFe₂O₄ nanoferrites, a well-known sol-gel auto-combustion technique was employed. All chemicals were purchased from Sigma Aldrich (AR grade, purity $\geq 99.9\%$). Stoichiometric amounts of precursors, cobalt nitrate hexahydrate, copper nitrate trihydrate, ferric nitrate nonahydrate, and citric acid were dissolved separately in 100 ml of distilled water. These aqueous solutions were stirred thoroughly to get transparent, homogeneous nitrate solutions. The obtained nitrate solutions were mixed together at 80–85°C. To neutralize the mixture, the pH was maintained at ~ 7 by pouring the droplets of ammonia solution. After continuous stirring for 5–6 h, a gel was formed. This gel combusts in a controlled way and produces a fluffy dark brownish powder. The obtained powder of CuFe₂O₄, Cu_{0.5}Co_{0.5}Fe₂O₄ and CoFe₂O₄ nanoferrites were ground thoroughly using a mortar and pestle and then annealed at 800°C for 2 h.

The synthesized samples were characterized by X-ray diffraction (XRD) (Rigaku Ltd., Japan) with a monochromatic radiation source of Cu-K α (wavelength ~ 1.541 Å) for structural and phase analysis. The surface morphology and the presence of elements with expected stoichiometric ratio were examined by scanning electron microscopy (SEM) and energy-dispersive x-ray (EDX) technique, respectively. A PerkinElmer Fourier transform infrared (FTIR) spectrophotometer was used to record the FTIR spectra in the range of 400–4000 cm⁻¹. A HORIBA Scientific spectrometer equipped with an Olympus confocal microscope was used to record the room temperature Raman spectra over the region 100–800 cm⁻¹. A PerkinElmer UV-visible spectrophotometer was used to record the absorption spectra of synthesized samples. To investigate the magnetic behavior, a Lake Shore model 7410 series vibrating-sample magnetometer (VSM) was used up to a magnetic field of ± 15 kOe at room temperature. The resistivity and dielectric properties of the samples were studied using a Keithley Electrometer model 6517B and an Agilent-4290 LCR meter interfaced with LabVIEW software, respectively.

Result and Discussion

XRD Analysis

Figure 1a, b and c depicts the Rietveld refined XRD pattern of CuFe₂O₄, Cu_{0.5}Co_{0.5}Fe₂O₄ and CoFe₂O₄ nanoferrites, respectively. The presence of sharp peaks in the

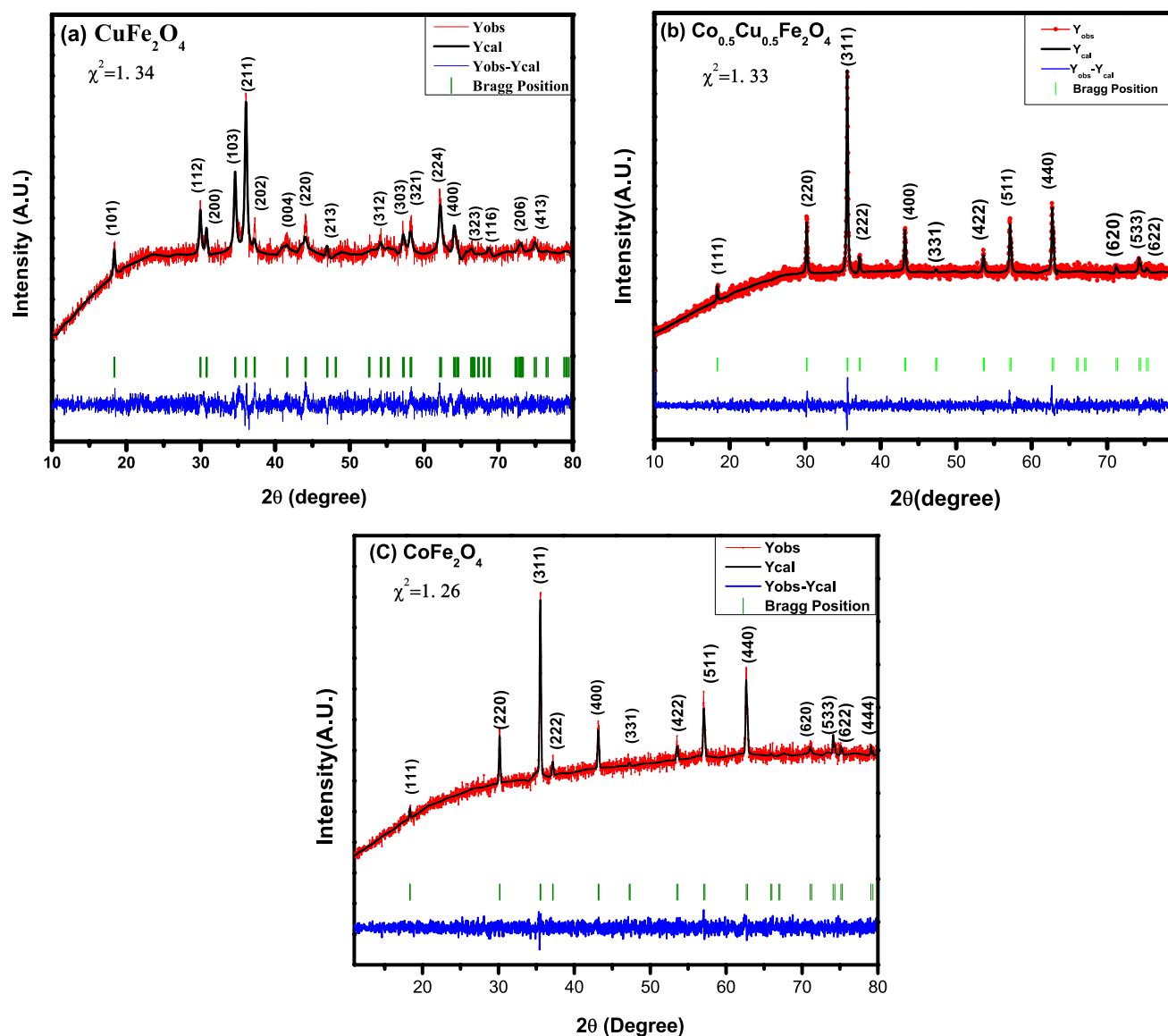


Fig. 1 Rietveld refinement of XRD pattern for (a) CuFe_2O_4 , (b) $\text{Cu}_{0.5}\text{Co}_{0.5}\text{Fe}_2\text{O}_4$, and (c) CoFe_2O_4 nanoferrites.

XRD pattern indicates the crystalline nature of synthesized nanoparticles. The XRD pattern confirmed the formation of tetragonal phase structure (space group I41/amd) for CuFe_2O_4 and cubic phase structure (space group Fd3m) for $\text{Cu}_{0.5}\text{Co}_{0.5}\text{Fe}_2\text{O}_4$ and CoFe_2O_4 nanoparticles. The peaks observed for CuFe_2O_4 , $\text{Cu}_{0.5}\text{Co}_{0.5}\text{Fe}_2\text{O}_4$ and CoFe_2O_4 nanoferrites were compared and satisfactorily indexed with JCPDS file no: 34-0425, 36-0153, and 22-1086, respectively. Further, to estimate different structural parameters, Rietveld refinement of XRD data is done by using FullProf software considering the I41/amd space group for CuFe_2O_4 (tetragonal) and Fd3m space group for $\text{Cu}_{0.5}\text{Co}_{0.5}\text{Fe}_2\text{O}_4$ and CoFe_2O_4 ferrites (cubic), respectively. XRD peak profiles were calculated using a pseudo-Voigt function.¹⁸ The refinement was done continuously until a goodness factor very

close to one was obtained. Table I shows the lattice parameters of direct and reciprocal space and the goodness factor (χ^2). The average crystallite size (D) was determined corresponding to the most intense diffraction peak (311) using the Debye-Scherrer formula. The formulas, which were used to calculate the crystallite size (D), x-ray density (ρ_x), interplanar spacing (d), and specific surface area (S) are taken from Ref. 29.

The structural parameters calculated by analyzing the XRD data are tabulated in Tables I and II. The average crystallite size is 25.26 ± 0.01 , 34.15 ± 0.02 , and 38.40 ± 0.02 nm for CuFe_2O_4 , $\text{Cu}_{0.5}\text{Co}_{0.5}\text{Fe}_2\text{O}_4$, and CoFe_2O_4 nanoferrites, respectively. The largest crystallite size for CoFe_2O_4 is expected due to large ionic radius of the Co^{+2} ion (0.74 Å) as compared to that of the Cu^{+2} (0.70 Å) ion.³⁰ X-ray density is

directly affected by the molecular weight and lattice parameter of the sample. The highest molecular weight of CuFe₂O₄ results in the largest x-ray density (10.81 ± 0.01 g cm⁻³) of CuFe₂O₄.

Williamson-Hall (W-H) method³¹ was also applied to determine the crystallite size (*D*) and microstructural lattice strain (ϵ) (Fig. 2). The positive sign of the slope indicates the tensile stress, while the negative sign shows the presence of compressive strain. It was observed that the sign of the slope for the CuFe₂O₄ sample is negative

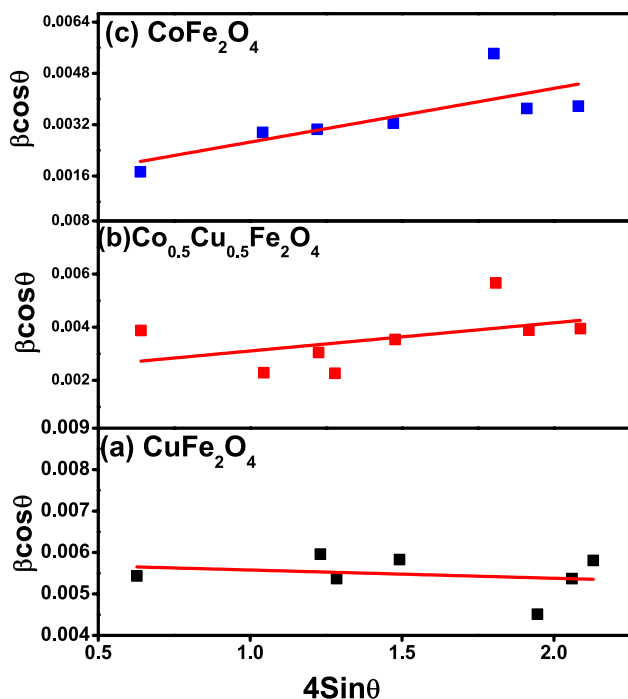


Fig. 2 Williamson-Hall (W-H) plot for (a) CuFe₂O₄, (b) Cu_{0.5}Co_{0.5}Fe₂O₄, and (c) CoFe₂O₄ nanoferrites.

while the sign is positive for Cu_{0.5}Co_{0.5}Fe₂O₄ and CoFe₂O₄ ferrite samples. The presence of compressive strain is also confirmed by the fact that in the CuFe₂O₄ sample, the value of crystallite size determined by W-H plot (23.09 ± 0.01 nm) is smaller than that determined by the Scherrer formula (25.26 ± 0.01 nm). However, for CoFe₂O₄, Cu_{0.5}Co_{0.5}Fe₂O₄ samples, the crystallite size obtained by the W-H plot is larger than that obtained by the Scherrer formula, which shows the presence of tensile strain.

To determine the cation distribution, the occupancy values of the cations for all samples were obtained after fitting XRD data using Rietveld refinement.¹⁸ The estimation of cations occupying the A and B sites were calculated by employing the least-squares refinement model. The cation distribution in ferrites is a function of various parameters such as radii of cations, thermal history, and particle size.³² The calculated cation distribution for CuFe₂O₄, Cu_{0.5}Co_{0.5}Fe₂O₄, and CoFe₂O₄ nanoparticles are presented in Table III. It is found that in CuFe₂O₄, Cu_{0.5}Co_{0.5}Fe₂O₄ and CoFe₂O₄ nanoferrites a remarkable fraction of metal ions occupy at A and B sites. Hence, the refinement result shows the presence of high content of divalent ion at the tetrahedral site in all the synthesized samples, which supports the formation of mixed spinel structure instead of inverse spinel structure.

The Bond_Str program³³ was used to estimate different bond lengths, which are shown in Table IV. From this table, it is interesting to note that for CuFe₂O₄, bond length Fe-O at the A site is highest while at the B site is smallest among all the samples. This may be due to the incorporation of more Fe⁺³ ions with small ionic radii (0.67 Å) at the A site and fewer Fe⁺³ at the B site in CuFe₂O₄ as compared to Cu_{0.5}Co_{0.5}Fe₂O₄ and CoFe₂O₄ ferrite samples.^{34,35} A similar result is observed in the bond length of the A and B sites of

Table I The Rietveld refined lattice parameter for CuFe₂O₄, Cu_{0.5}Co_{0.5}Fe₂O₄, and CoFe₂O₄ nanoferrites

Sample	Direct lattice parameter				Reciprocal lattice parameter				χ^2
	a (Å) ±0.002	b (Å) ±0.002	c (Å) ±0.002	V (Å ³)	a* (Å ⁻¹) ±0.002	b* (Å ⁻¹) ±0.002	c* (Å ⁻¹) ±0.002	V* (Å ⁻³) 0.0001	
CuFe ₂ O ₄	5.813	5.813	8.685	293.488 ± 0.269	0.172	0.172	0.115	0.0034	1.34
Cu _{0.5} Co _{0.5} Fe ₂ O ₄	8.380	8.380	8.380	588.712 ± 0.421	0.119	0.119	0.119	0.0016	1.33
CoFe ₂ O ₄	8.382	8.382	8.382	588.981 ± 0.421	0.119	0.119	0.119	0.0016	1.26

Table II Structural parameters of CuFe₂O₄, Cu_{0.5}Co_{0.5}Fe₂O₄, and CoFe₂O₄ nanoferrites calculated from XRD data

Sample	Crystallite size (nm)		Lattice strain × 10 ⁻⁴	X-ray density (g/cm ³)	Specific surface area (m ² /g)
	By Scherrer	By W-H Plot			
CuFe ₂ O ₄	25.26 ± 0.01	23.09 ± 0.01	1.98 ± 0.02	10.81 ± 0.01	22.59 ± 0.03
Cu _{0.5} Co _{0.5} Fe ₂ O ₄	34.15 ± 0.02	46.12 ± 0.03	1.41 ± 0.26	5.38 ± 0.01	32.61 ± 0.03
CoFe ₂ O ₄	38.40 ± 0.02	52.62 ± 0.03	1.67 ± 0.23	5.31 ± 0.01	29.41 ± 0.04

Table III Distribution of cations for CuFe_2O_4 , $\text{Cu}_{0.5}\text{Co}_{0.5}\text{Fe}_2\text{O}_4$ and CoFe_2O_4 nanoferrites

Sample	Cation distribution
CuFe_2O_4	$(\text{Cu}^{+2}_{0.45}\text{Fe}^{+3}_{0.55})_A [\text{Cu}^{+2}_{0.55}\text{Fe}^{+3}_{1.45}]_B$
$\text{Cu}_{0.5}\text{Co}_{0.5}\text{Fe}_2\text{O}_4$	$(\text{Cu}^{+2}_{0.26}\text{Co}^{+2}_{0.31}\text{Fe}^{+3}_{0.43})_A$ $[\text{Cu}^{+2}_{0.25}\text{Co}^{+2}_{0.18}\text{Fe}^{+3}_{1.57}]_B$
CoFe_2O_4	$(\text{Co}^{+2}_{0.68}\text{Fe}^{+3}_{0.32})_A [\text{Co}^{+2}_{0.32}\text{Fe}^{+3}_{1.68}]_B$

CuFe_2O_4 by the substitution of In^{+3} ion³⁶ and the reported value of bond length is comparable to that of present work.

SEM and EDX

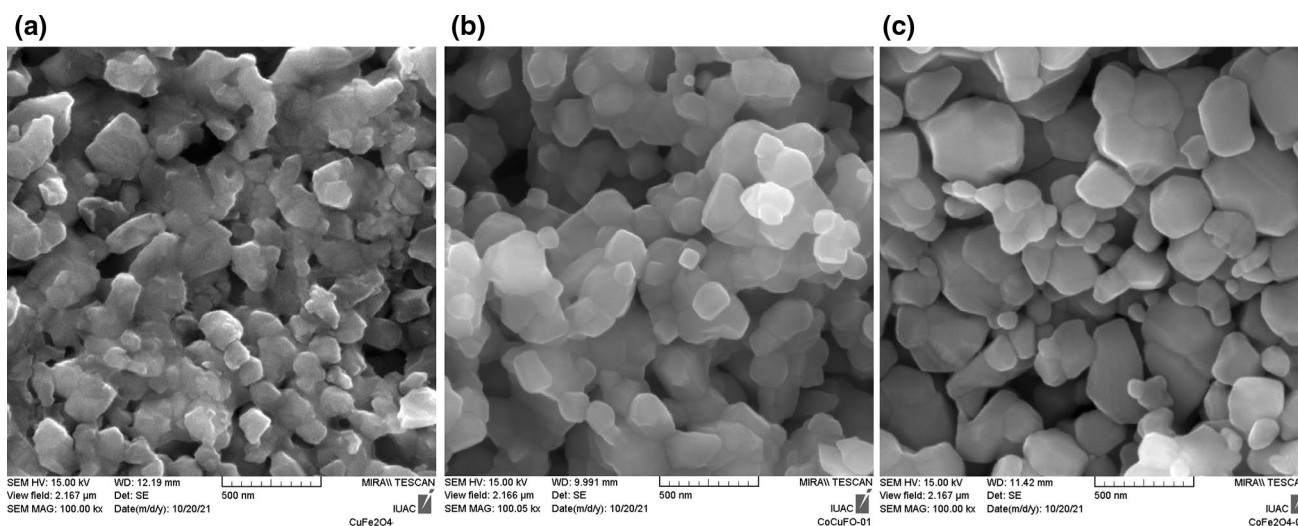
Figures 3a, b, c and 4a, b and c represent the SEM micrograph and particle size histograms of CuFe_2O_4 , $\text{Cu}_{0.5}\text{Co}_{0.5}\text{Fe}_2\text{O}_4$, and CoFe_2O_4 nanoferrite, respectively. The SEM micrographs indicate the agglomeration of small sized irregular shaped particles. The enhancement in surface-to-volume ratio of nanostructured materials usually causes this agglomeration.³⁷ It could also be attributed

to the grain growth mechanism involving diffusion coefficients, sintering temperature, and the concentration of different ions.³⁸ The particle size is calculated using Image J software. The average particle size is found to be 142 ± 2 , 166 ± 2 and 152 ± 2 nm for CuFe_2O_4 , $\text{Cu}_{0.5}\text{Co}_{0.5}\text{Fe}_2\text{O}_4$ and CoFe_2O_4 , respectively. The obtained particle size is larger in comparison to crystallite size, as calculated by XRD data (Table II), due to agglomeration of particles which consist of many crystallites.

EDX spectroscopy is carried out to examine the quantitative elemental analysis of synthesized samples. The EDX spectra are shown in Fig. 5a, b and c, and the numerical output is listed in the Table V. The proportion of constituent elements revealed by EDX output is approximately the same as the chemical composition of respective ferrite samples. The peaks corresponding to the constituent elements Fe, Co, Cu, and O are seen in EDX spectra, confirming the purity of the samples. However, an extra Au peak is also observed which is due to the thin coating of Au on the sample surface to make it conducting.

Table IV Bond length of CuFe_2O_4 , $\text{Cu}_{0.5}\text{Co}_{0.5}\text{Fe}_2\text{O}_4$, and CoFe_2O_4 nanoferrites

	CuFe_2O_4		$\text{Cu}_{0.5}\text{Co}_{0.5}\text{Fe}_2\text{O}_4$		CoFe_2O_4	
	Bond type	Distance ± 0.01 (Å)	Bond type	Distance ± 0.01 (Å)	Bond type	Distance ± 0.01 (Å)
1	Fe(A)-O	2.11	Fe(A)-O	1.72	Fe(A)-O	1.88
2	Fe(B)-O	1.90	Fe(B)-O	1.99	Fe(B)-O	2.27
3	Cu(A)-O	2.27	Cu(A)-O	1.86	–	–
4	Cu(B)-O	1.88	Cu(B)-O	2.32	–	–
5	–	–	Co(A)-O	1.85	Co(A)-O	1.90
6	–	–	Co(B)-O	2.11	Co(B)-O	2.15

**Fig. 3** SEM micrographs for (a) CuFe_2O_4 , (b) $\text{Cu}_{0.5}\text{Co}_{0.5}\text{Fe}_2\text{O}_4$, and (c) CoFe_2O_4 nanoferrites.

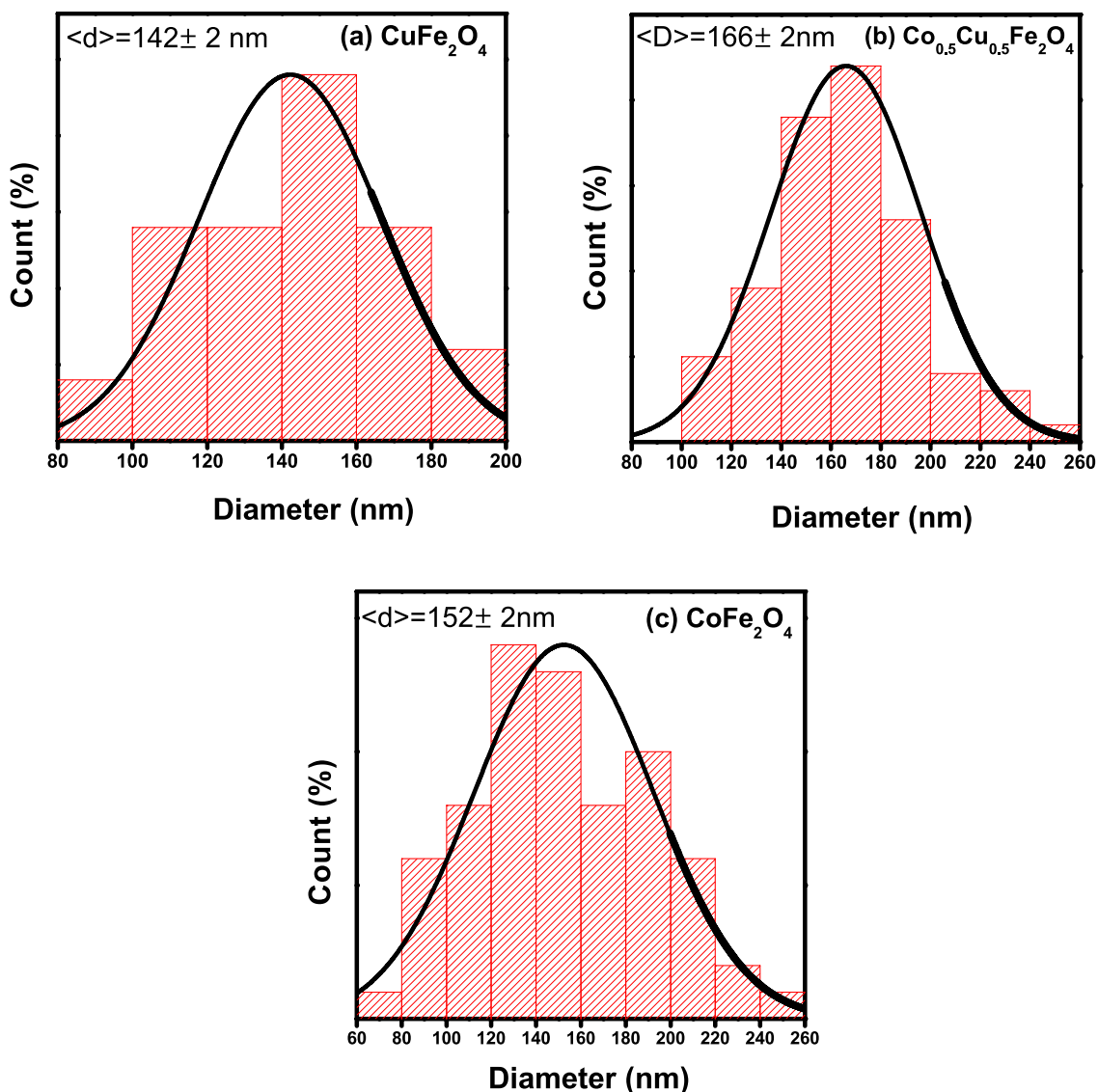


Fig. 4 Particle size histograms for (a) CuFe₂O₄, (b) Cu_{0.5}Co_{0.5}Fe₂O₄, and (c) CoFe₂O₄ nanoferrites.

FTIR Spectroscopy

FTIR spectroscopy is an effective technique for identifying different functional groups in materials. The FTIR spectra were recorded in the range of 400–4000 cm⁻¹ as shown in Fig. 6. Waldron proposed that the vibration band in the range of 350–450 and 500–600 cm⁻¹ correspond to metal–oxygen at octahedral and tetrahedral sites, respectively.³⁹

Presently, due to the instrument's limitation, the vibration bands below 400 cm⁻¹ could not be observed and single band corresponding to the tetrahedral site is observed at 572 ± 1, 579 ± 1, and 581 ± 1 cm⁻¹ for CuFe₂O₄, Cu_{0.5}Co_{0.5}Fe₂O₄, and CoFe₂O₄ nanoferrites respectively. However, in the case of CuFe₂O₄, the band corresponding

to the octahedral site is also observed at 426 ± 1 cm⁻¹, which disappeared in Cu_{0.5}Co_{0.5}Fe₂O₄ and CoFe₂O₄ samples, indicating the lower value of band position at the octahedral site. The IR band position depends on variation in bond length, ionic radii, mass, position, and interatomic forces between vibrating atoms at respective sites.^{40,41} The cation distribution confirmed the increasing pattern of molecular weight at the tetrahedral site for CuFe₂O₄, Cu_{0.5}Co_{0.5}Fe₂O₄, and CoFe₂O₄ nanoferrites which support the observed trend in band position at tetrahedral sites. The vibration band near 1385 cm⁻¹ represents the presence of the NO₃⁻² group. The band corresponding to 1644 cm⁻¹ and 3406 cm⁻¹ represent the vibrations associated with the –OH group.^{42–44}

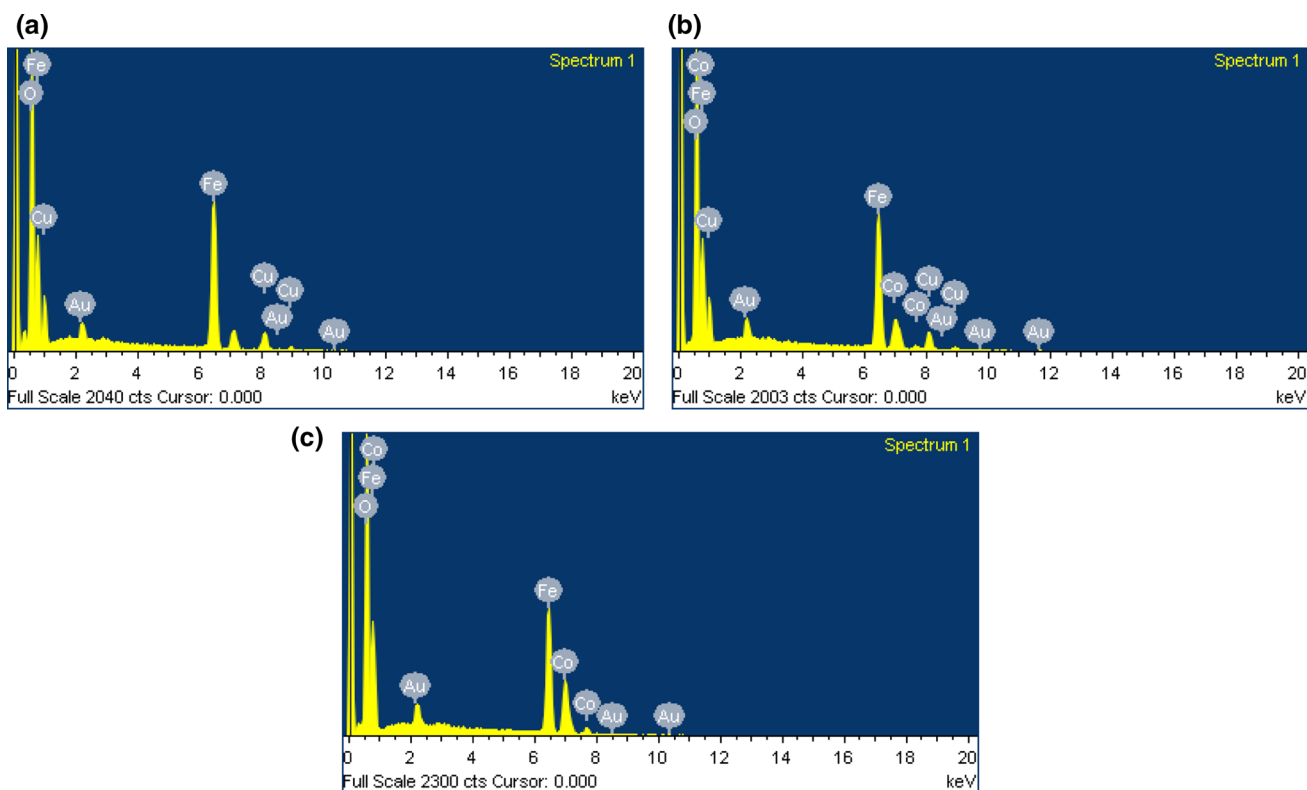


Fig. 5 EDX Analysis for (a) CuFe_2O_4 , (b) $\text{Cu}_{0.5}\text{Co}_{0.5}\text{Fe}_2\text{O}_4$, and (c) CoFe_2O_4 nanoferrites.

Table V Elemental composition of CuFe_2O_4 , $\text{Cu}_{0.5}\text{Co}_{0.5}\text{Fe}_2\text{O}_4$, and CoFe_2O_4 nanoferrites

Elements	CuFe_2O_4		$\text{Cu}_{0.5}\text{Co}_{0.5}\text{Fe}_2\text{O}_4$		CoFe_2O_4	
	Weight%	Atomic %	Weight%	Atomic %	Weight%	Atomic %
Cu	15.39	7.93	14.12	7.03	–	–
Co	–	–	12.33	7.49	25.04	14.06
Fe	55.55	32.85	46.28	27.96	46.80	27.72
O	29.06	59.49	27.27	57.52	28.16	58.22
Total	100%		100%		100%	

Raman Spectroscopy

Figure 7a, b and c shows the Raman spectra of CuFe_2O_4 , $\text{Cu}_{0.5}\text{Co}_{0.5}\text{Fe}_2\text{O}_4$, and CoFe_2O_4 nanoferrites in the range of 100 to 800 cm^{-1} . According to group theory, five Raman modes, $A_{1g} + E_g + 3T_{2g}$, are associated with cubic spinel, and ten modes, $2A_{1g} + 3B_{1g} + B_{2g} + 4E_{2g}$, are associated with the tetragonal structure.⁴⁵ In the present study, we observed six Raman modes ($1A_{1g}$, $1B_{2g}$, $3B_{1g}$, and E_{2g}) for tetragonal structure (CuFe_2O_4) and five Raman active modes ($1A_{1g}$, $1E_g$, and $3T_{2g}$) for cubic structure ($\text{Cu}_{0.5}\text{Co}_{0.5}\text{Fe}_2\text{O}_4$ and CoFe_2O_4) in the range of 100 – 800 cm^{-1} . The recorded Raman spectra confirmed the presence of Raman vibrational modes as expected in the case of tetragonal and cubic spinel ferrites. The A_{1g} mode is due to the symmetric stretching vibration of oxygen-metal ions present at the tetrahedral site,

whereas the modes (B_{1g} , B_{2g} , E_{2g} , etc.) at lower wavenumber are ascribed to the phonon vibrations corresponding to symmetric and antisymmetric bending of oxygen ions with respect to metal ions present at the octahedral site.⁴⁵

Fityk software⁴⁶ was used for peak profile fitting, and best fit was observed for the Gaussian-type profile. Information such as peak center, full width at half maximum (FWHM), and area of individual Raman modes thus obtained is shown in Table VI. The band position of Raman vibrational mode associated with tetrahedral sites are at higher wavenumber for $\text{Cu}_{0.5}\text{Co}_{0.5}\text{Fe}_2\text{O}_4$ and CoFe_2O_4 samples in comparison to the CuFe_2O_4 system. This variation in band position of Raman modes is because vibrational frequency depends on both the bond strength and the reduced mass of the vibrating species.^{47,48} On the other hand, in all the samples, the position of Raman modes at the octahedral site is lower in

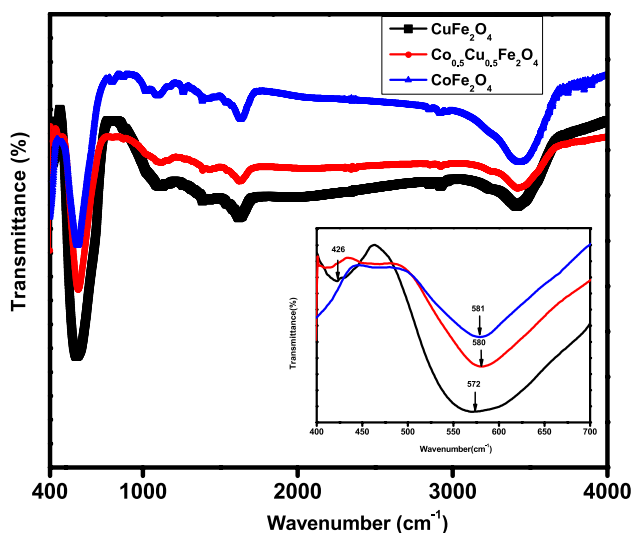


Fig. 6 FTIR spectra for CuFe₂O₄, Cu_{0.5}Co_{0.5}Fe₂O₄, and CoFe₂O₄ nanoferrites.

comparison to the tetrahedral site, which represents the presence of a higher effective mass at octahedral sites. A similar result is confirmed by the observed wavenumber shifting in FTIR spectra, which is well supported by the cation distribution analysis as discussed earlier.

UV–Visible Spectroscopy

The optical properties of synthesized nanoferrites were demonstrated by recording the absorption spectra in the wavelength range of 200–800 nm as depicted in Fig. 8a. The absorption maxima were strong in the visible region around the wavelength range of 500–600 nm for all the samples. A small kink observed at 400 nm for all three samples is due to the change of a deuterium light source (ultraviolet range) to a tungsten-halogen source (visible range).

The value of the optical band gap depends on various factors such as crystallite size, structural parameters, annealing temperature, displacement of atoms, lattice defects, carrier concentration, and the presence of impurities.⁴⁹ The electronic transition takes place between the valence band (O 2*p* states) to the conduction band (Fe 3*d*). The optical band gap energies for synthesized CuFe₂O₄, Cu_{0.5}Co_{0.5}Fe₂O₄, and CoFe₂O₄ nanoferrites were calculated by using the Tauc plot (Fig. 8b). The Tauc plot represents the incident photon energy (*hν*) on the X-axis and (*αhν*)^{*m*} on the Y-axis, where *α* is the absorption coefficient of materials, *m* represents the type of transition.⁵⁰ The value of *m* can be 2, 1/2, 3, and 3/2, which indicates direct allowed, direct forbidden, indirect allowed, and indirect forbidden transitions, respectively. The intercept on the X-axis after extrapolation of the linear region of the Tauc plot gives the value of optical band gap energy.

Considering the synthesized nanoferrites as a direct band gap material^{51,52} the calculated values of the band gap for CuFe₂O₄, Cu_{0.5}Co_{0.5}Fe₂O₄, and CoFe₂O₄ nanoferrites came out to be 1.58 ± 0.02 eV, 1.18 ± 0.02 eV, and 1.01 ± 0.02 eV, respectively. In the present work, the smallest band gap of CoFe₂O₄ is expected due to its largest average crystallite size which results in the reduction of grain boundaries. Subsequently, the decreased scattering of carriers at grain boundaries leads to the small band gap energy.⁵¹ The value of direct optical band gap was 1.59 eV and 1.11 eV as proposed by Gupta et al. for tetragonal structured CuFe₂O₄ and CoFe₂O₄ nanoparticles with an average crystallite size of 16 and 34 nm, respectively.⁵² In the present work, the obtained values of band gap are lower than that reported in Ref. 52 for both CuFe₂O₄ and CoFe₂O₄ nanoparticles, which may be attributed to the larger crystallite size of synthesized samples in comparison to reported work. Tatarchuk et al. reported the optical properties of Co-Zn ferrites and observed that the estimated optical band gap decreased significantly from 1.89 eV to 1.31 eV with the increase in Co⁺² concentration, and crystallite size was found to increase from 37 nm to 51 nm.⁵³ A similar trend is observed in the present work, i.e. the band gap is smaller for the sample with a larger crystallite size.

Magnetic Study

The M-H hysteresis curves for CuFe₂O₄, Cu_{0.5}Co_{0.5}Fe₂O₄, and CoFe₂O₄ nanoferrites examined by VSM measurement at room temperature are shown in Fig. 9 and the obtained magnetic parameters are summarized in Table VII. The saturation magnetization and coercivity for synthesized nanoferrites are in the range of 45.07–80.06 emu/g with an error of 0.02 and 182.45–959.10 Oe with an error of ±0.30, respectively. Magnetic parameters crucially depend on the arrangement, concentration, occupancy, anisotropy, additives, and exchange interaction of cations at A and B sites.^{54,55} The magnetic moment (*η*), anisotropy constant (*K*), and squareness ratio (*S*) are calculated using the relations⁵⁶ given below:

$$\eta = \frac{M \times M_s}{5585}, K = \frac{M_s \times H_c}{0.96}, S = \frac{M_r}{M_s} \quad (1)$$

Here *M* is the molecular weight of the sample, *M_s*, *M_r*, and *H_c* are the saturation magnetization (emu g⁻¹), retentivity (emu g⁻¹), and coercivity (Oe), respectively.

The large value of magnetic parameters for Cu_{0.5}Co_{0.5}Fe₂O₄ and CoFe₂O₄ nanoferrites can be explained mainly by the presence of highly magnetic Co⁺² ions with a magnetic moment of 3μ_B in comparison to 1μ_B for Cu⁺² ions.¹⁴ The cation distribution in CuFe₂O₄, Cu_{0.5}Co_{0.5}Fe₂O₄,

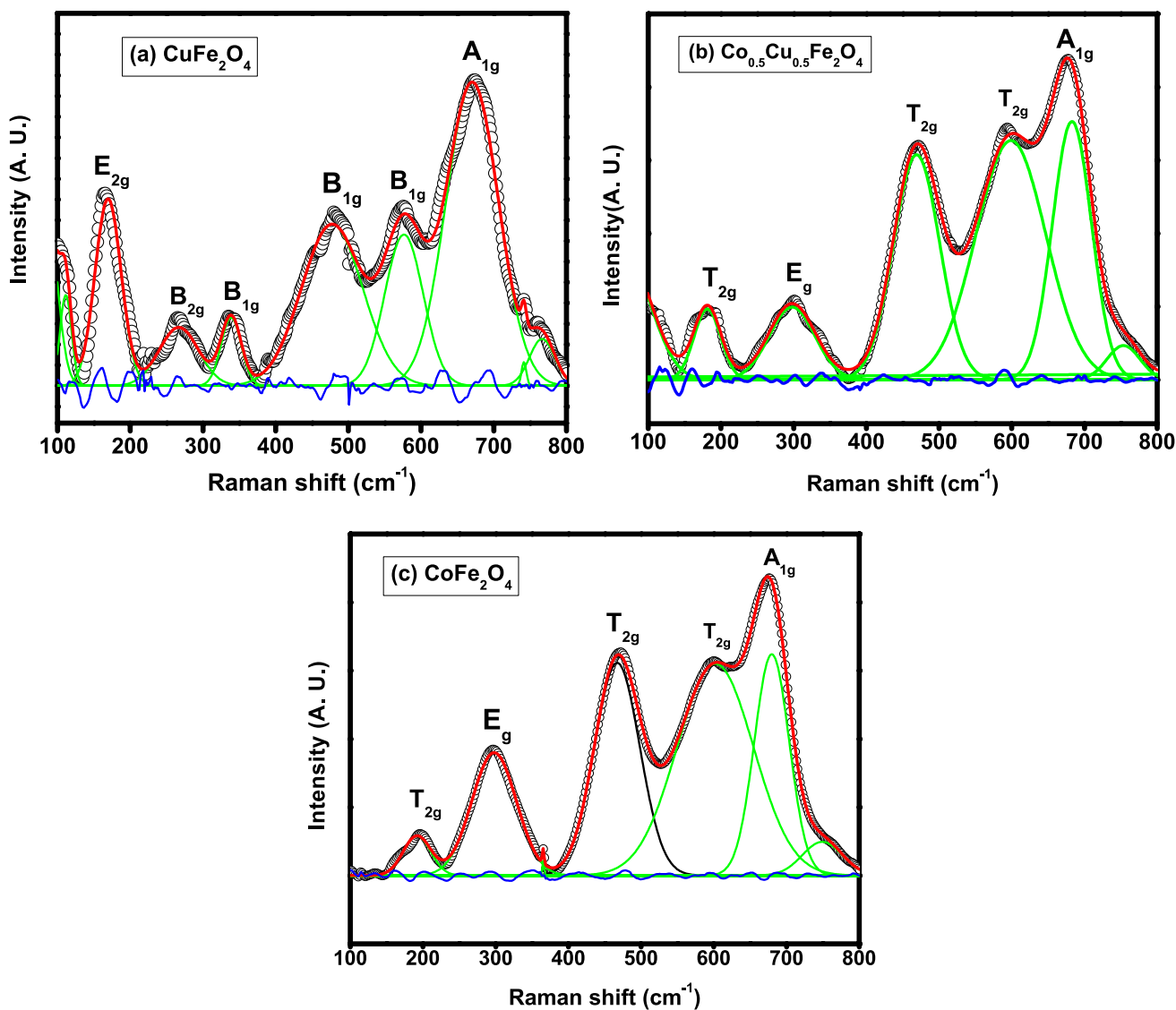


Fig. 7 Raman spectra for (a) CuFe_2O_4 , (b) $\text{Cu}_{0.5}\text{Co}_{0.5}\text{Fe}_2\text{O}_4$, and (c) CoFe_2O_4 nanoferrites.

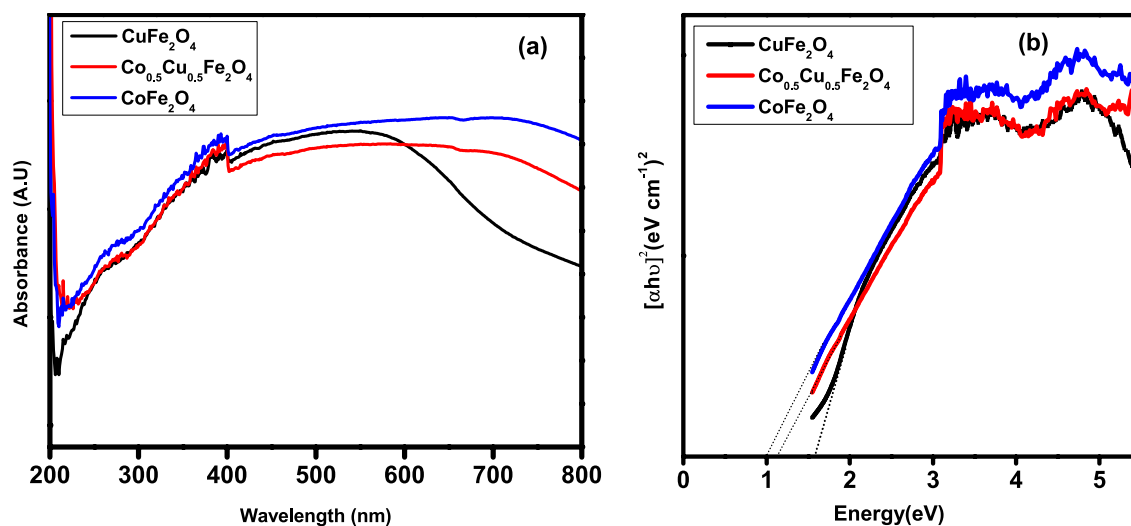
and CoFe_2O_4 ferrite systems, obtained by Rietveld refinement also supports the obtained pattern of M_s in three samples. Based on Neel's two-sublattice model, magnetic moments for synthesized ferrites are calculated theoretically using the cation distribution obtained by Rietveld refinement. As can be seen from Table VII, the theoretical magnetic moment calculated by cation distribution follow a similar trend as the experimental magnetic moment obtained by VSM measurement. The quantitative difference between these values can be because of not an exact antiparallel arrangement between the spins of A and B site cations or the role of spin canting.

The lowest values of M_s and H_c for CuFe_2O_4 are attributed to the lower magneto-crystalline anisotropy and the weaker magnetic moment of Cu^{+2} ions compared to Co^{+2}

ions. The highest value M_s for CoFe_2O_4 is because of its largest crystallite size. The larger crystallite size consists of many magnetic domains. In the presence of an external magnetic field, the magnetic domain tends to be aligned in the direction of the field. Magnetic materials with a large number of domains give rise to large values of M_s . Moreover, the energy required for the alignment of large number of domains in particular direction is higher.⁵⁴ Therefore, samples with larger crystallite size are expected to have high anisotropy energy as observed in the present study. A similar trend was observed for magnetic parameters with variation in crystallite size for $\text{Ni}_{1-x}\text{Zn}_x\text{Fe}_2\text{O}_4$ ($x=0.0, 0.3, 0.5, \& 0.7$) by Costa et al.,⁵⁷ for $\text{Ni}_{0.7}\text{Mn}_{0.3}\text{Gd}_x\text{Fe}_{2-x}\text{O}_4$ ferrites by Zhao et al.,⁵⁸ for Mg-Zn ferrite by Choodamani et al.⁵⁹

Table VI Raman band position for CuFe₂O₄, Cu_{0.5}Co_{0.5}Fe₂O₄ and CoFe₂O₄ nanoferrites

Sample	Raman modes	Peak center (cm ⁻¹)	Area (A.U.)	FWHM (cm ⁻¹)
CuFe ₂ O ₄	E _{2g}	169	2031.14	42.243
	B _{2g}	266	964.42	64.14
	B _{1g}	338	571.73	32.538
	B _{1g}	477	4116.99	99.085
	B _{1g}	576	2431.06	62.502
	A _{1g}	670	6666.04	85.402
Cu _{0.5} Co _{0.5} Fe ₂ O ₄	T _{2g}	181	2229.93	43.265
	E _g	297	3906.87	73.924
	T _{2g}	469	12,264	74.911
	T _{2g}	598	19,743.2	113.44
	A _{1g}	682	11,894.9	63.306
	T _{2g}	191	2750.05	44.5878
CoFe ₂ O ₄	E _g	297	13,855.6	72.3469
	T _{2g}	466	24,376.6	73.5235
	T _{2g}	596	40,864.8	123.79
	A _g	679	19,481	56.463

**Fig. 8** (a) UV-Visible absorption spectra; (b) Tauc's plot for CuFe₂O₄, Cu_{0.5}Co_{0.5}Fe₂O₄, and CoFe₂O₄ nanoferrites.

The change in coercivity may originate from the effect of spin canting, the exchange anisotropy and the change in superexchange interactions.⁶⁰ The higher saturation magnetization and coercivity lead to large anisotropy coefficient of Cu_{0.5}Co_{0.5}Fe₂O₄ and CoFe₂O₄ samples than the CuFe₂O₄ system. The highest value of coercivity and squareness ratio is achieved for Cu_{0.5}Co_{0.5}Fe₂O₄ ($H_c = 959.10 \pm 0.30$ Oe and $S = 0.45 \pm 0.05$) samples, which makes them suitable candidates for high-density recording media.

Electrical Properties

Resistivity Measurement

To carry out electrical measurements powders were ground and pressed into circular shaped pellets of 10 mm in diameter and ~2 mm in thickness using a hydraulic press pelletizer. The electrical behavior of the CuFe₂O₄,

$\text{Cu}_{0.5}\text{Co}_{0.5}\text{Fe}_2\text{O}_4$, and CoFe_2O_4 nanoferrites was examined by measuring dc resistivity (ρ) as a function of temperature using the Four-probe technique. The variation in dc resistivity in the temperature range 100–400 K is shown in Fig. 10. The plot shows that by increasing the temperature, the resistivity of all synthesized nanoferrites decreases, hence the conductivity increases. The transportation of electrons takes place between Fe^{+2} and Fe^{+3} ions, resulting in thermally activated charge interaction, whose drift velocity increased with temperature during the hopping process, which might be the reason for the increased conductivity of synthesized nanoferrites with increasing temperatures.⁶¹

Moreover, it is noticed that the resistivity of $\text{Cu}_{0.5}\text{Co}_{0.5}\text{Fe}_2\text{O}_4$ and CoFe_2O_4 sample is less in comparison to CuFe_2O_4 nanoparticles. The observed values of resistivity at 300 K for CuFe_2O_4 , $\text{Cu}_{0.5}\text{Co}_{0.5}\text{Fe}_2\text{O}_4$, and CoFe_2O_4 nanoferrites are $(6.03 \pm 0.28) \times 10^7$, $(4.01 \pm 0.20) \times 10^7$ and $(2.11 \pm 0.03) \times 10^7 \Omega\text{cm}$, respectively. The variation in resistivity can be explained by the Verwey conduction mechanism.⁶² From cation distribution, as mentioned in Table III,

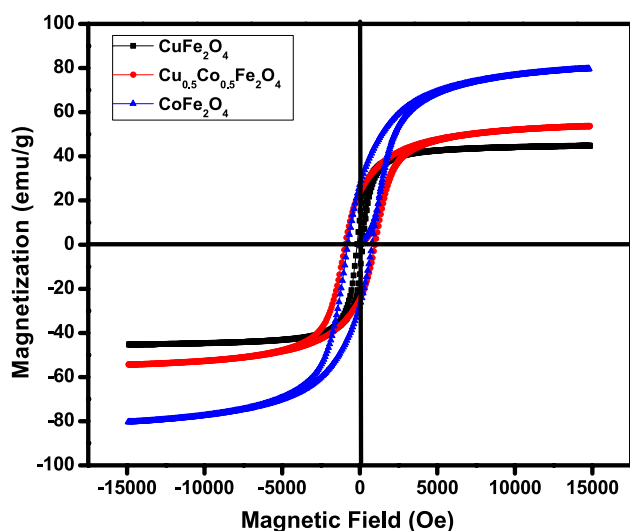


Fig. 9 Hysteresis curve of CuFe_2O_4 , $\text{Cu}_{0.5}\text{Co}_{0.5}\text{Fe}_2\text{O}_4$, and CoFe_2O_4 nanoferrites.

it can be seen that in $\text{Cu}_{0.5}\text{Co}_{0.5}\text{Fe}_2\text{O}_4$ and CoFe_2O_4 nanoferrites, more Fe^{+3} ions are present at *B* sites in comparison to the CuFe_2O_4 system; therefore, more electron hopping takes place between ferric (Fe^{+3}) and ferrous (Fe^{+2}) ions in $\text{Cu}_{0.5}\text{Co}_{0.5}\text{Fe}_2\text{O}_4$ and CoFe_2O_4 ferrite samples, causing the low resistivity or higher conductivity.^{63,64}

The variation in resistivity can also be understood on the basis of crystallite size. The sample with the smaller crystallite size contains a larger number of grain boundaries. These grain boundaries act as a barrier for the movement of charge carriers.⁶⁵ In the present work, the calculated crystallite size of CuFe_2O_4 (25 nm) is less in comparison to $\text{Cu}_{0.5}\text{Co}_{0.5}\text{Fe}_2\text{O}_4$ (34 nm) and CoFe_2O_4 (38 nm) ferrites. Therefore, the resistivity of CuFe_2O_4 is higher among the synthesized samples. The present outcomes are consistent with previous studies conducted by Venkataraju et al. for $\text{Mn}_{0.5-x}\text{Ni}_x\text{Zn}_{0.5}\text{Fe}_2\text{O}_4$ ($x=0.0, 0.1, 0.2, 0.3$ and 0.5),⁶⁶ Shinde et al. for $\text{Ni}_{1-x}\text{Zn}_x\text{Fe}_2\text{O}_4$ ($x=0.0, 0.2, 0.4, 0.6, 0.8$, and 1.0).⁶⁷ Thus, the decreasing order of resistivity for

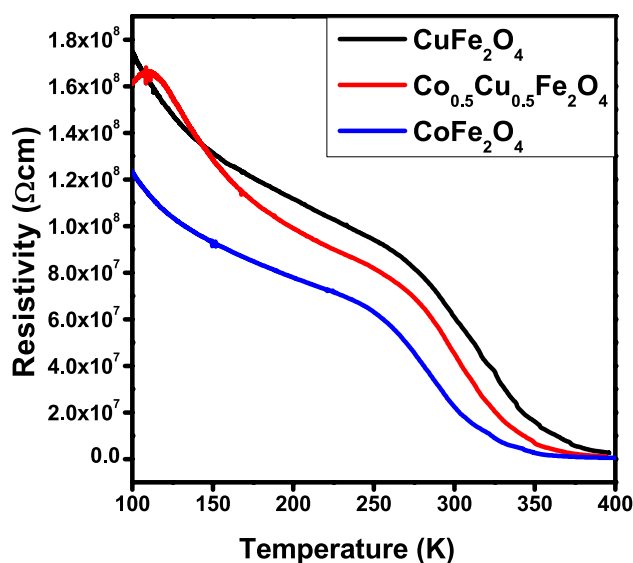


Fig. 10 Variation in resistivity as a function temperature for CuFe_2O_4 , $\text{Cu}_{0.5}\text{Co}_{0.5}\text{Fe}_2\text{O}_4$, and CoFe_2O_4 nanoferrites.

Table VII Magnetic parameters of CuFe_2O_4 , $\text{Cu}_{0.5}\text{Co}_{0.5}\text{Fe}_2\text{O}_4$, and CoFe_2O_4 nanoferrites

Magnetic parameters	CuFe_2O_4	$\text{Cu}_{0.5}\text{Co}_{0.5}\text{Fe}_2\text{O}_4$	CoFe_2O_4
Saturation magnetization (emu/g)	45.07 ± 0.02	53.99 ± 0.02	80.06 ± 0.02
Coercivity (Oe)	182.45 ± 0.30	959.10 ± 0.30	779.44 ± 0.30
Retentivity (emu/g)	12.66 ± 0.03	24.16 ± 0.03	27.40 ± 0.03
Squareness ratio	0.27 ± 0.05	0.45 ± 0.05	0.33 ± 0.05
<i>Magnetic moment (μ_B)</i>			
By VSM measurement	1.93 ± 0.02	2.29 ± 0.02	3.36 ± 0.02
By cation distribution	4.28 ± 0.02	5.73 ± 0.02	6.21 ± 0.02
Anisotropy coefficient $\times 10^3$ (erg/cm ³)	8.56 ± 0.32	53.93 ± 0.32	65.02 ± 0.32

CuFe₂O₄, Cu_{0.5}Co_{0.5}Fe₂O₄ and CoFe₂O₄ is attributed to increasing order of their crystallite size.

Dielectric Measurement

The dielectric measurement was done over the temperature range of 100–400 K and the frequency range 50 Hz to 2 MHz as shown in Figs. 11 and 12. It can be seen that temperature, frequency, and substitution of additives influence the dielectric properties of ferrites. The silver coating was done on opposite faces of the pellets to make the parallel plate capacitor geometry with ferrite material as the dielectric medium. The dielectric constant (ϵ') and dielectric loss ($\tan\delta$) of the samples have been calculated using the formula mentioned in Ref. 55

Variation in dielectric properties of the materials according to crystallite size can be explained on the basis of Maxwell–Wagner and Koops models.⁶⁸ According to these models, the smaller crystallite size means smaller grains and a larger grain boundary. Ferrite nanoparticles consist of well-conducting grains separated by resistive grain boundaries. If the resistance of grain boundary is high enough then charge carriers are piled up at the grain boundaries. The accumulation of charge at the grain boundary leads to a high dielectric constant of the material. In the present study, due to the smallest crystallite size, CuFe₂O₄ has highly resistive grain boundaries. Therefore, it has the highest dielectric constant among the studied samples. The trend of dielectric constant with crystallite size was reported by Yousuf et al.⁶⁹ for yttrium-substituted manganese ferrite (MnY_xFe_{2-x}O₄). Their study is consistent with the result of the present work that the smallest crystallite size of CuFe₂O₄ leads to the

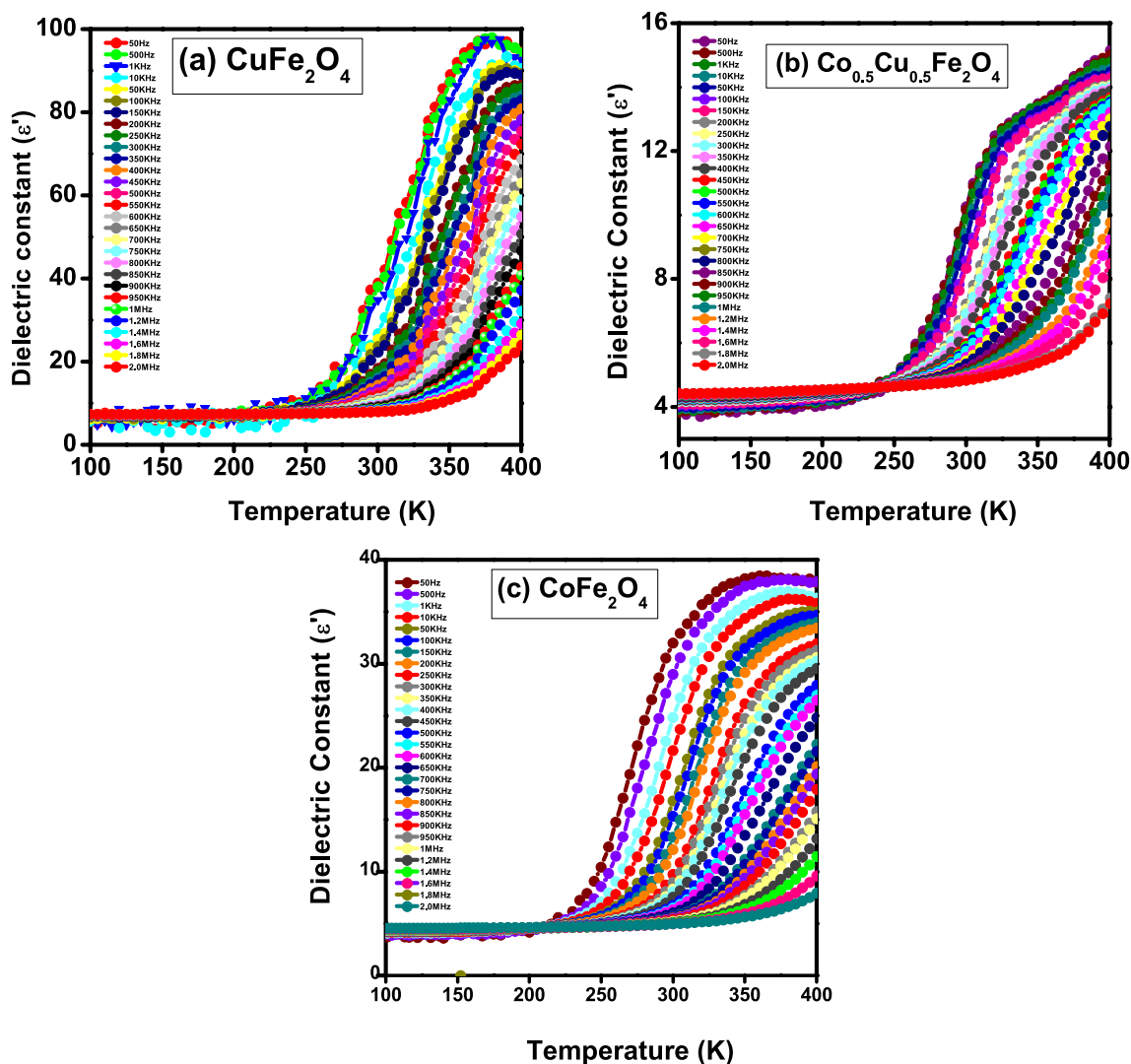


Fig. 11 Variation in dielectric constant (ϵ') as a function of temperature for (a) CuFe₂O₄, (b) Cu_{0.5}Co_{0.5}Fe₂O₄, and (c) CoFe₂O₄ nanoferrites.

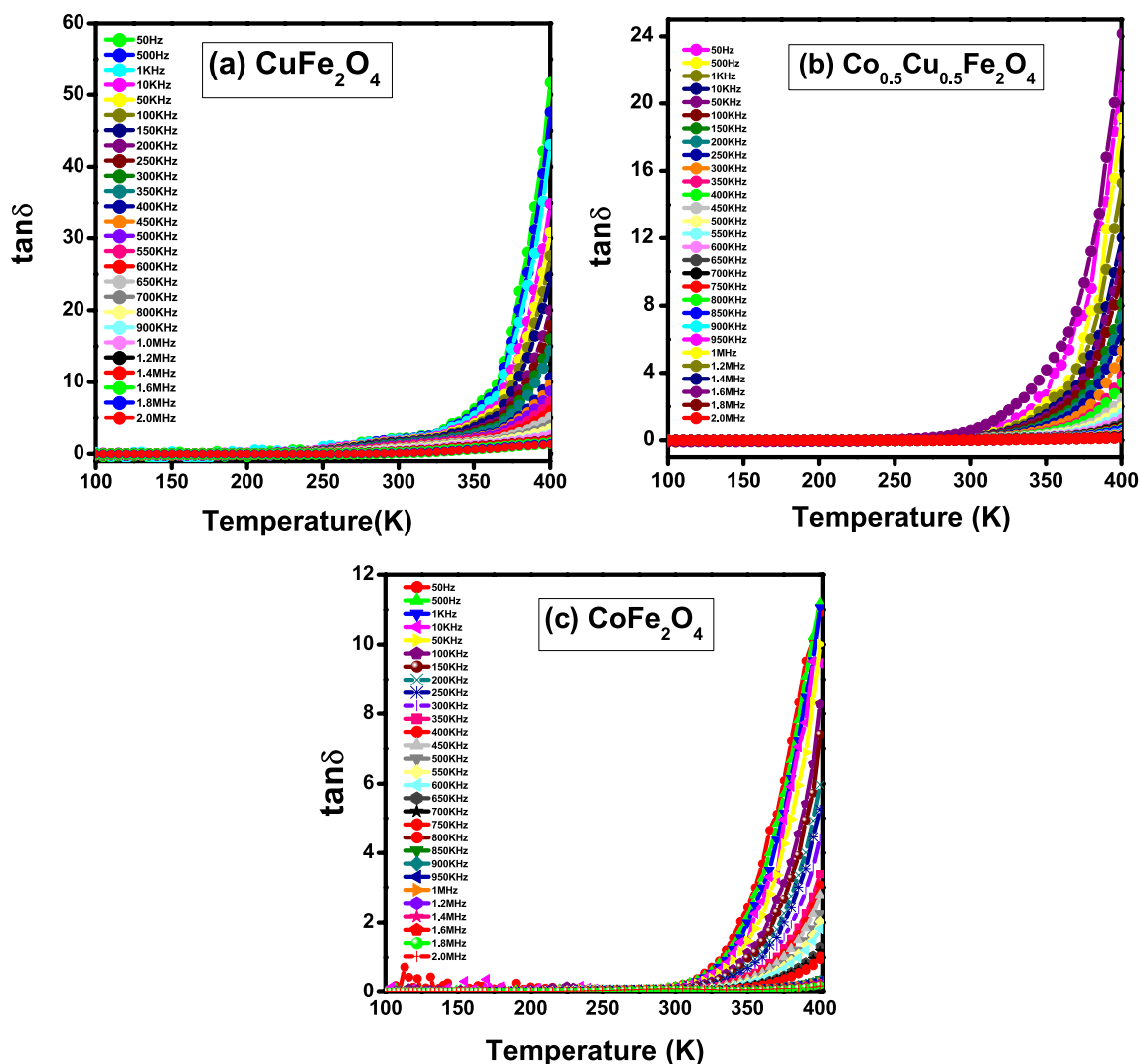


Fig. 12 Variation in loss tangent ($\tan\delta$) as a function of temperature for (a) CuFe_2O_4 , (b) $\text{Cu}_{0.5}\text{Co}_{0.5}\text{Fe}_2\text{O}_4$, and (c) CoFe_2O_4 nanoferrites.

highest dielectric constant. However, the observed values of dielectric constant for $\text{Cu}_{0.5}\text{Co}_{0.5}\text{Fe}_2\text{O}_4$ and CoFe_2O_4 ferrite show a pattern opposite to the crystallite size. The crystallite size and dielectric constant of $\text{Cu}_{0.5}\text{Co}_{0.5}\text{Fe}_2\text{O}_4$ ($D \sim 34.15 \pm 0.02$ nm) is less in comparison to that of CoFe_2O_4 ($D \sim 38.40 \pm 0.02$ nm). This observed trend in dielectric constant might be due to some other factors such as microstructure, interfacial dislocations, homogeneity, or imperfections distribution of cations.⁷⁰ The collective behavior of dielectric constant with temperature and frequency is discussed below.

The real part of the dielectric constant (ϵ') and tangent loss ($\tan\delta$) remains almost constant at lower temperatures, while it starts to increase monotonically with an increase in temperature. A similar trend of the temperature-dependent dielectric constant and dielectric loss has been reported in the case of different spinel ferrites.^{3,4} At low temperatures,

the thermal energy provided to the sample is insufficient to raise the mobility of charge carriers, and as a result, there is less hopping and polarization. However, by further raising the temperature, the increasing values of dielectric constant for all frequencies can be accredited to the enhanced mobility of thermally activated charge carriers.

The temperature dependence of ϵ' is different at different frequencies. At lower frequencies, ϵ' increases more rapidly as compared to that at higher frequencies. The contribution of interfacial, dipolar, ionic, and electronic polarization results in the dielectric constant of material.¹² The interfacial and dipolar polarizations have strong dependence on temperature, as well as frequency which is the reason behind the rapid increase in dielectric constant at low frequencies. On the other hand, it is noticed that at higher frequencies, the change in polarization becomes insignificant. This behavior is due to the presence of both electronic and ionic

polarization, which remains almost independent of temperature and frequency.⁷¹

It is noticed that the value of the dielectric constant (ϵ') and dielectric loss tangent ($\tan\delta$) is higher for the CuFe₂O₄ ferrite system in comparison to Cu_{0.5}Co_{0.5}Fe₂O₄ and CoFe₂O₄ ferrites. The Cu_{0.5}Co_{0.5}Fe₂O₄ nanoparticles have the smallest value of dielectric constant (ϵ'). In Cu_{0.5}Co_{0.5}Fe₂O₄, the contribution of both Cu⁺² and Co⁺² ions provides a higher limit to the movement of Fe⁺³ ions leading to the decrease in polarization, and hence dielectric constant.³ The temperature dependence of dielectric constant as a function of frequency exhibits dielectric maxima for CuFe₂O₄ and CoFe₂O₄ samples. However, for Cu_{0.5}Co_{0.5}Fe₂O₄ ferrites, the dielectric maxima shift at the higher temperature, above 400 K. It can be seen from Fig. 10, that the dielectric tangent loss is less for Cu_{0.5}Co_{0.5}Fe₂O₄ and CoFe₂O₄ samples as compared to CuFe₂O₄ ferrites. Magnetic materials with low dielectric tangent loss are important for the electronic systems involved in high-frequency applications. Hence, CoFe₂O₄ and Cu_{0.5}Co_{0.5}Fe₂O₄ with low dielectric loss may be recommended for effective use in high-frequency data storage applications.

Conclusions

CuFe₂O₄, Cu_{0.5}Co_{0.5}Fe₂O₄, and CoFe₂O₄ samples were prepared using sol-gel auto-combustion. XRD pattern confirmed the tetragonal phase structure of CuFe₂O₄ and cubic structure of Cu_{0.5}Co_{0.5}Fe₂O₄ and CoFe₂O₄ ferrite system. The distribution of cations obtained by Full Prof software confirmed the formation of mixed spinel nanoferrites. The observed shift in the FTIR and Raman spectra supports the result obtained by XRD analysis and the cation distribution. The highest values of coercivity and squareness ratio were observed for Cu_{0.5}Co_{0.5}Fe₂O₄ nanoferrite, which makes it suitable for magnetic applications such as magnetic data storage devices and magnetic tapes in comparison to CuFe₂O₄ and CoFe₂O₄ ferrites. The variation in resistivity with temperature represents the semiconducting nature, which is also supported by the calculated band gap of synthesized nanoferrites. The low value of dielectric loss in Cu_{0.5}Co_{0.5}Fe₂O₄ and CoFe₂O₄ suggests that the synthesized nanoferrites are promising candidates to be used in power transformers at high frequencies.

Acknowledgments One of the authors, Reena Dhyani, is thankful to TEQIP-III, College of Technology, G.B. Pant University of Agriculture & Technology, Pantnagar, for providing the scholarship to carry out this research work. The authors also acknowledge IUAC for support of research work. Reena Dhyani sincerely acknowledges the help and suggestions received from Mr. R. C. Meena IUAC, New Delhi.

Conflict of interest The authors declare that they do not have conflict of interest.

References

1. M.A. Gabal, Y.M. Al Angari, and F.A. Al-Agel, Cr-Substituted Ni-Zn Ferrites via Oxalate Decomposition. Structural, Electrical and Magnetic Properties. *J. Magn. Magn. Mater.* 391, 108–115 (2015). <https://doi.org/10.1016/j.jmmm.2015.04.115>.
2. C.S. Pawar, M.P. Gujar, and V.L. Mathe, Optical Properties of Spin-Deposited Nanocrystalline Ni-Zn Ferrite Thin Films Processed by Sol-Gel. *J. Supercond. Nov. Magn.* 30, 615–625 (2017). <https://doi.org/10.1007/s10948-016-3720-y>.
3. P. Kumar, S.K. Sharma, M. Knobel, and M. Singh, Effect of La⁺³ Doping on the Electric, Dielectric and Magnetic Properties of Cobalt Ferrite Processed by Co-precipitation Technique. *J. Alloys Compd.* 508, 115 (2010). <https://doi.org/10.1016/j.jallcom.2010.08.007>.
4. P.S. Rawat, R.C. Srivastava, G. Dixit, G.C. Joshi, and K. Asokan, Facile Synthesis and Temperature Dependent Dielectric Properties of MnFe₂O₄ Nanoparticles. *AIP Conf. Proceed.* 2115, 030104 (2019). <https://doi.org/10.1063/1.5112943>.
5. M.H. Abdellatif, C. Innocenti, I. Liakos, A. Scarpellini, S. Marras, and M. Salerno, Effect of Jahn-Teller Distortion on the Short Range Magnetic Order in Copper Ferrite. *J. Magn. Magn. Mater.* 424, 402 (2017). <https://doi.org/10.1016/j.jmmm.2016.10.110>.
6. A.M. Balagurov, I.A. Bobrikov, V.Y. Pomjakushin, D.V. Sheptyakov, and V.Y. Yushankhai, Interplay Between Structural and Magnetic Phase Transitions in Copper Ferrite Studied with High-Resolution Neutron Diffraction. *J. Magn. Magn. Mater.* 374, 591 (2015). <https://doi.org/10.1016/j.jmmm.2014.08.092>.
7. A. Paul and R. Mandal, Scope and Possibilities of Copper Based Semiconducting Materials in Optoelectronic Applications-A Review. *Invertis J. Renew. Energy* 7, 106 (2017). <https://doi.org/10.5958/2454-7611.2017.00015.7>.
8. S. Anandan, T. Selvamani, G.G. Prasad, A.M. Asiri, and J.J. Wu, Magnetic and Catalytic Properties of Inverse Spinel CuFe₂O₄ Nanoparticles. *J. Magn. Magn. Mater.* 432, 437 (2017). <https://doi.org/10.1016/j.jmmm.2017.02.026>.
9. M.A. Haija, A.F. Abu-Hani, N. Hamdan, S. Stephen, and A.I. Ayesh, Characterization of H₂S Gas Sensor based on CuFe₂O₄ Nanoparticles. *J. Alloys Compd.* 690, 461 (2017). <https://doi.org/10.1016/j.jallcom.2016.08.174>.
10. X. Cao, K. Sun, C. Sun, and L. Leng, The Study on Microstructure and Microwave-Absorbing Properties of Lithium Zinc Ferrites Doped with Magnesium and Copper. *J. Magn. Magn. Mater.* 321, 2896 (2009). <https://doi.org/10.1016/j.jmmm.2009.04.049>.
11. K.K. Kefeni, T.A. Msagati, and B.B. Mamba, Ferrite Nanoparticles: Synthesis, Characterisation and Applications in Electronic Device. *Mater. Sci. Eng. B* 215, 37 (2017). <https://doi.org/10.1016/j.mseb.2016.11.002>.
12. D.P. Sherstyuk, A.Y. Starikov, V.E. Zhivulin, D.A. Zherebtsov, S.A. Gudkova, N.S. Perov, and A.V. Trukhanov, Effect of Co Content on Magnetic Features and SPIN States in Ni-Zn Spinel Ferrites. *Ceram. Int.* 47, 12163 (2021). <https://doi.org/10.1016/j.ceramint.2021.01.063>.
13. R. Kumar, H. Kumar, R.R. Singh, and P.B. Barman, Variation in Magnetic and Structural Properties of Co-doped Ni-Zn Ferrite Nanoparticles: a Different Aspect. *J. Sol-Gel Sci. Tech.* 78, 566 (2016). <https://doi.org/10.1007/s10971-016-3984-5>.
14. V.S. Sawant and K.Y. Rajpure, The Effect of Co Substitution on the Structural and Magnetic Properties of Lithium Ferrite Synthesized by an Auto Combustion Method. *J. Magn. Magn. Mater.* 382, 152 (2015). <https://doi.org/10.1016/j.jmmm.2015.01.064>.

15. C. Singh, S. Bindra-Narang, I.S. Hudiara, and Y. Bai, The Effect of Co and Zr Substitution on dc Magnetic Properties of Ba–Sr Ferrite. *J. Alloys Compd.* 464, 429 (2008). <https://doi.org/10.1016/j.jallcom.2007.10.009>.
16. C.F. Zhang, X.C. Zhong, H.Y. Yu, Z.W. Liu, and D.C. Zeng, Effects of Cobalt Doping on the Microstructure and Magnetic Properties of Mn–Zn Ferrites Prepared by the Co-precipitation Method. *Phys. B Cond. Matter.* 404, 2327 (2009). <https://doi.org/10.1016/j.physb.2008.12.044>.
17. A.G. Abraham, A. Manikandan, E. Manikandan, S. Vadivel, S.K. Jaganathan, A. Baykal, and P.S. Renganathan, Enhanced Magneto-Optical and Photo-Catalytic Properties of Transition Metal Cobalt (Co⁺² Ions) Doped Spinel MgFe₂O₄ Ferrite Nanocomposites. *J. Magn. Magn. Mater.* 452, 380 (2018). <https://doi.org/10.1016/j.jmmm.2018.01.001>.
18. L. Kumar, P. Kumar, and M. Kar, Cation Distribution by Rietveld Technique and Magnetocrystalline Anisotropy of Zn Substituted Nanocrystalline Cobalt Ferrite. *J. Alloys Compd.* 551, 72 (2013). <https://doi.org/10.1016/j.jallcom.2012.10.009>.
19. G. Dixit, R.C. Singh, H.M. Srivastava, and Agrawal, Magnetic Resonance Study of Ce and Gd Doped NiFe₂O₄ Nanoparticles. *J. Magn. Magn. Mater.* 324, 479 (2012). <https://doi.org/10.1016/j.jmmm.2011.08.027>.
20. A. Zainal Dedi, Manaf, Microstructure and Microwave Absorption Characteristics of BaTiO₃-CoFe₂O₄ Composites. *Key Eng. Mater.* 855, 322 (2020).
21. R. Dhyani and R.C. Srivastava, Structural and Magnetic Study of Co_{0.5}Cu_{0.5}Fe₂O₄/Polypyrrole Nanocomposites. *J. Emerg. Technol. Innov. Res.* 6, 291 (2019).
22. P.S. Rawat, R.C. Srivastava, G. Dixit, and K. Asokan, Structural, Functional and Magnetic Ordering Modifications in Graphene Oxide and Graphite by 100 MeV Gold Ion Irradiation. *Vacuum* 182, 109700 (2020). <https://doi.org/10.1016/j.vacuum.2020.109700>.
23. A.S. Hamed, I.A. Ali, M. El Ghazaly, M. Al-Abyad, and H.E. Hassan, Nanocomposites of ZnO Mixed with Different Ni-Ferrite Contents: Structural and Magnetic Properties. *Phys. B Condens. Mater.* 607, 412861 (2021). <https://doi.org/10.1016/j.physb.2021.412861>.
24. M.A. Ahmed, S.F. Mansour, and M.A. Abdo, Characterization and Dramatic Variations of the Magnetic Properties of Cu-Doped Nanometric Co Ferrite. *Phys. Scr.* 84, 055602 (2011).
25. El-Masry, M. El-Shahat, R. Ramadan, and R.M. Abdelhameed, Selective Photocatalytic Reduction of Nitroarenes into Amines based on Cobalt/Copper Ferrite and Cobalt-Doped Copper Ferrite Nano-Photocatalyst. *J. Mater. Sci. Mater. Electron.* 32, 18408 (2021). <https://doi.org/10.1007/s10854-021-06387-3>.
26. S. Rehman, M.A. Ansari, M.A. Alzohairy, M.N. Alomary, B.R. Jermy, R. Shahzad, and Z.H. Alsalem, Antibacterial and Antifungal Activity of Novel Synthesized Neodymium-Substituted Cobalt Ferrite Nanoparticles for Biomedical Application. *Processes* 7, 714 (2019). <https://doi.org/10.3390/pr7100714>.
27. S. Bhaskaran, I.A. Al-Omari, and E.V. Gopalan, On the Enhanced Coercive Field and Anisotropy Observed in Cobalt Substituted Copper Ferrite Nanoparticles Prepared by a Modified Sol-Gel Method. *J. Alloys Compd.* 884, 161095 (2021). <https://doi.org/10.1016/j.jallcom.2021.161095>.
28. M.A. Dar and D. Varshney, Effect of d-Block Element Co⁺² Substitution on Structural, Mössbauer and Dielectric Properties of Spinel Copper Ferrites. *J. Magn. Magn. Mater.* 436, 101 (2017). <https://doi.org/10.1016/j.jmmm.2017.04.046>.
29. R. Jabbar, S.H. Sabeeh, and A.M. Hameed, Structural, Dielectric and Magnetic Properties of Mn⁺² Doped Cobalt Ferrite Nanoparticles. *J. Magn. Magn. Mater.* 494, 165726 (2020). <https://doi.org/10.1016/j.jmmm.2019.165726>.
30. M. Hashim, S. Kumar, B.H. Koo, S.E. Shirsath, E.M. Mohammed, J. Kumar, and R. Shah, Structural, Electrical and Magnetic Properties of Co–Cu Ferrite Nanoparticles. *J. Alloys Compd.* 518, 11 (2012). <https://doi.org/10.1016/j.jallcom.2011.12.017>.
31. R. Vishwaroop and S.N. Mathad, Synthesis, Structural, WH Plot and Size-Strain Analysis of Nano Cobalt Doped MgFe₂O₄ Ferrite. *Sci. Sinter.* 52, 349 (2020). <https://doi.org/10.2298/SOS2003349V>.
32. Z. Karimi, Y. Mohammadifar, H. Shokrollahi, S.K. Asl, G. Yousefi, and L. Karimi, Magnetic and Structural Properties of Nano Sized Dy-Doped Cobalt Ferrite Synthesized by Co-precipitation. *J. Magn. Magn. Mater.* 361, 150 (2014). <https://doi.org/10.1016/j.jmmm.2014.01.016>.
33. I.D. Brown, *The Chemical Bond in Inorganic Chemistry—The Bond Valence Model. IU Cr monographs on Crystallography 12* (Oxford: Oxford University Press, 2002).
34. M. Prasad, B.R. Babu, K.V. Ramesh, and K. Trinath, Structural and Magnetic Studies on Chromium Substituted Ni-Zn Nano Ferrite Synthesized by Citrate Gel Auto Combustion Method. *J. Supercond. Nov. Magn.* 27, 2735 (2014). <https://doi.org/10.1007/s10948-014-2637-6>.
35. J.A. Gomes, M.H. Sousa, F.A. Tourinho, J. Mestnik-Filho, R. Itri, and J. Depeyrot, Rietveld Structure Refinement of the Cation Distribution in Ferrite Fine Particles Studied by X-ray Powder Diffraction. *J. Magn. Magn. Mater.* 289, 184 (2005). <https://doi.org/10.1016/j.jmmm.2004.11.053>.
36. M. Junaid, M.A. Khan, S.A. Abubshait, M.N. Akhtar, N.A. Kattan, A. Laref, and H.M.A. Javed, Structural, Spectral, Dielectric and Magnetic Properties of Indium Substituted Copper Spinel Ferrites Synthesized via Sol Gel Technique. *Ceram. Int.* 46, 27410 (2020). <https://doi.org/10.1016/j.ceramint.2020.07.227>.
37. N. Kumar, R.K. Singh, and H.K. Satyapal, Structural, Optical, and Magnetic Properties of Non-stoichiometric Lithium Substituted Magnesium Ferrite Nanoparticles for Multifunctional Applications. *J. Mater. Sci. Mater. Electron.* 31, 9231 (2020). <https://doi.org/10.1007/s10854-020-03454-z>.
38. S. Sagadevan, Z.Z. Chowdhury, and R.F. Rafique, Preparation and Characterization of Nickel Ferrite Nanoparticles via Co-precipitation Method. *Mater. Res.* (2018). <https://doi.org/10.1590/1980-5373-MR-2016-0533>.
39. R. Sharma, P. Thakur, M. Kumar, N. Thakur, N.S. Negi, P. Sharma, and V. Sharma, Improvement in Magnetic Behaviour of Cobalt Doped Magnesium Zinc Nano-ferrites via Co-precipitation Route. *J. Alloys Compd.* 684, 569 (2016). <https://doi.org/10.1016/j.jallcom.2016.05.200>.
40. V. Kumar, N. Kumar, S.B. Das, R.K. Singh, K. Sarkar, and M. Kumar, Sol-Gel Assisted Synthesis and Tuning of Structural, Photoluminescence, Magnetic and Multiferroic Properties by Annealing Temperature in Nanostructured Zinc Ferrite. *Mater. Today Proc.* (2021). <https://doi.org/10.1016/j.matpr.2021.05.215>.
41. T.M. Hammad, J.K. Salem, A.A. Amsaha, and N.K. Hejazy, Optical and Magnetic Characterizations of Zinc Substituted Copper Ferrite Synthesized by a Co-precipitation Chemical Method. *J. Alloys Compd.* 741, 123 (2018). <https://doi.org/10.1016/j.jallcom.2018.01.123>.
42. G. Dixit, J.P. Singh, R.C. Srivastava, and H.M. Agrawal, Structural, Optical and Magnetic Studies of Ce Doped NiFe₂O₄ Nanoparticles. *J. Magn. Magn. Mater.* 345, 65 (2013). <https://doi.org/10.1016/j.jmmm.2013.05.060>.
43. J.P. Singh, G. Dixit, R.C. Srivastava, H.M. Agrawal, and R. Kumar, Raman and Fourier-Transform Infrared Spectroscopic Study of Nanosized Zinc Ferrite Irradiated with 200 MeV Ag⁺¹⁵ Beam. *J. Alloys Compd.* 551, 370 (2013). <https://doi.org/10.1016/j.jallcom.2012.10.006>.
44. Z. Wang, R.T. Downs, V. Pischedda, R. Shetty, S.K. Saxena, C.S. Zha, and A. Waskowska, High-Pressure X-ray Diffraction and Raman Spectroscopic Studies of the Tetragonal Spinel CoFe₂O₄.

- Phys. Rev. B* 68, 094101 (2003). <https://doi.org/10.1103/PhysRevB.68.094101>.
45. S. Joshi, M. Kumar, S. Chhoker, G. Srivastava, M. Jewariya, and V.N. Singh, Structural, Magnetic, Dielectric and Optical Properties of Nickel Ferrite Nanoparticles Synthesized by Co-precipitation Method. *J. Mol. Struct.* 1076, 55 (2014). <https://doi.org/10.1016/j.molstruc.2014.07.048>.
 46. M. Wojdyr, Fityk: a General-Purpose Peak Fitting Program. *J. Appl. Crystallogr.* 43, 1126–1128 (2010).
 47. S. Thota, S.C. Kashyap, S.K. Sharma, and V.R. Reddy, Micro Raman, Mossbauer and Magnetic Studies of Manganese Substituted Zinc Ferrite Nanoparticles: Role of Mn. *J. Phys. Chem. Solids* 91, 136–144 (2016). <https://doi.org/10.1016/j.jpcs.2015.12.013>.
 48. M.P. Ghosh and S. Mukherjee, Microstructural, Magnetic, and Hyperfine Characterizations of Cu-Doped Cobalt Ferrite Nanoparticles. *J. Am. Ceram. Soc.* 102, 7509–7520 (2019). <https://doi.org/10.1111/jace.16687>.
 49. M.A. Almessiere, Y. Slimani, S. Güner, M. Nawaz, A. Baykal, F. Aldakheel, and B.E.K.İR. Ozcelik, Magnetic and Structural Characterization of Nb³⁺ Substituted CoFe₂O₄ Nanoparticles. *Ceram. Int.* 45, 8222–8232 (2019). <https://doi.org/10.1016/j.ceramint.2019.01.125>.
 50. J. Tauc, *Optical Properties of Amorphous Semiconductors Amorphous and Liquid Semiconductors* (Boston: Springer, 1974), pp. 159–220. <https://doi.org/10.1007/978-1-4615-8705-74>.
 51. S. Anjum, J. Fayyaz, R. Khurram, and R. Zia, Tuning of Magnetic and Optical Properties of Co_{0.8}Zn_{0.2}Fe₂O₄ Spinel Ferrite Thin Films Based on Post Annealing Temperature. *J. Supercond. Nov. Magn.* 31, 4095 (2018). <https://doi.org/10.1007/s10948-018-4662-3>.
 52. N.K. Gupta, Y. Ghaffari, S. Kim, J. Bae, K.S. Kim, and M. Saifuddin, Photocatalytic Degradation of Organic Pollutants Over MFe₂O₄ (M= Co, Ni, Cu, Zn) Nanoparticles at Neutral pH. *Sci. Rep.* 10, 1 (2020). <https://doi.org/10.1038/s41598-020-61930-2>.
 53. T.R. Tatarchuk, N.D. Paliychuk, M. Bououdina, B. Al-Najar, M. Pacia, W. Macyk, and A. Shyichuk, Effect of Cobalt Substitution on Structural, Elastic, Magnetic and Optical Properties of Zinc Ferrite Nanoparticles. *J. Alloys Compd.* 731, 1256 (2018). <https://doi.org/10.1016/j.jallcom.2017.10.103>.
 54. A.A. Ati, Z. Othaman, and A. Samavati, Influence of Cobalt on Structural and Magnetic Properties of Nickel Ferrite Nanoparticles. *J. Mol. Struct.* 1052, 177 (2013). <https://doi.org/10.1016/j.molstruc.2013.08.040>.
 55. N.I. Dedi, T. Kristiantoro, G.F.N. Alam, and N. Sudrajat, Magnetic Properties of Cobalt Ferrite Synthesized by Mechanical Alloying. *AIP Conf. Proceed.* 1964, 020003 (2018).
 56. S. Munir, I. Ahmad, A. Laref, and H.M.T. Farid, Synthesis, Structural, Dielectric and Magnetic Properties of Hexagonal Ferrites. *Appl. Phys. A* 126, 1 (2020). <https://doi.org/10.1007/s00339-020-03809-7>.
 57. A.C.F.M. Costa, V.J. Silva, D.R. Cornejo, M.R. Morelli, R.H.G.A. Kiminami, and L. Gama, Magnetic and Structural Properties of NiFe₂O₄ Ferrite Nanopowder Doped with Zn. *J. Magn. Magn. Mater.* 320, 370 (2008). <https://doi.org/10.1016/j.jmmm.2008.02.159>.
 58. L. Zhao, Y. Cui, H. Yang, L. Yu, W. Jin, and S. Feng, The Magnetic Properties of Ni_{0.7}Mn_{0.3}GdxFe_{2-x}O₄ Ferrite. *Mater. Lett.* 60, 104–108 (2006). <https://doi.org/10.1016/j.matlet.2005.07.083>.
 59. C. Choodamani, G.P. Nagabhushana, B. Rudraswamy, and G.T. Chandrappa, Thermal Effect on Magnetic Properties of Mg-Zn Ferrite Nanoparticles. *Mater. Lett.* 116, 227 (2014). <https://doi.org/10.1016/j.matlet.2013.11.024>.
 60. U. Ghazanfar, S.A. Siddiqi, and G. Abbas, Study of Room Temperature dc Resistivity in Comparison with Activation Energy and Drift Mobility of NiZn Ferrites. *Mater. Sci. Eng. B* 118, 132 (2005). <https://doi.org/10.1016/j.mseb.2004.12.086>.
 61. A.M.A. Henaish, O.M. Hemeda, B.I. Salem, F.S. El-Sbakhy, and T. Khalass, Structural, Magnetic and Electrical Properties of Nano NiCr_xFe_{2-x}O₄ Synthesized by Flash Auto Combustion Method. *J. Phys. Conf. Series* 1253, 012025 (2019). <https://doi.org/10.1088/1742-6596/1253/1/012025>.
 62. E.J.W. Verwey, P.W. Haaijman, F.C. Romeijn, and G.W. Vanosterhout, Controlled-Valency Semiconductors. *Philips Res. Rep.* 5, 173 (1950).
 63. S. Nasir, G. Asghar, M.A. Malik, and M. Anis-ur-Rehman, Structural, Dielectric and Electrical Properties of Zinc Doped Nickel Nanoferrites Prepared by Simplified Sol-Gel Method. *J. Sol Gel Sci. Technol.* 59, 111 (2011). <https://doi.org/10.1007/s10971-011-2468-x>.
 64. C.C. Chauhan, A.R. Kagdi, R.B. Jotania, A. Upadhyay, C.S. Sandhu, S.E. Shirsath, and S.S. Meena, Structural, Magnetic and Dielectric Properties of Co-Zr Substituted M-type Calcium Hexagonal Ferrite Nanoparticles in the Presence of α-Fe₂O₃ Phase. *Ceram. Int.* 44, 17812 (2018). <https://doi.org/10.1016/j.ceramint.2018.06.249>.
 65. D.H. Zhang and H.L. Ma, Scattering Mechanisms of Charge Carriers in Transparent Conducting Oxide Films. *Appl. Phys. A* 62, 487 (1996). <https://doi.org/10.1007/BF01567122>.
 66. C. Venkataraju, G. Sathish Kumar, and K. Sivakumar, Effect of Nickel on the Electrical Properties of Nanostructured MnZn Ferrite. *J. Alloys Compd.* 498, 203 (2010). <https://doi.org/10.1016/j.jallcom.2010.03.160>.
 67. T.J. Shinde, A.B. Gadkari, and P.N. Vasambekar, DC Resistivity of Ni-Zn Ferrites Prepared by Oxalate Precipitation Method. *Mater. Chem. Phys.* 111, 87 (2008). <https://doi.org/10.1016/j.matchemphys.2008.03.028>.
 68. C.G. Koops, On the Dispersion of Resistivity and Dielectric Constant of Some Semiconductors at Audio Frequencies. *Phys. Rev.* 83, 121 (1951). <https://doi.org/10.1103/PhysRev.83.121>.
 69. M.A. Yousuf, M.M. Baig, N.F. Al-Khalli, M.A. Khan, M.F.A. Aboud, I. Shakir, and M.F. Warsi, The Impact of Yttrium Cations (Y³⁺) on Structural, Spectral and Dielectric Properties of Spinel Manganese Ferrite Nanoparticles. *Ceram. Int.* 45, 10936 (2019). <https://doi.org/10.1016/j.ceramint.2019.02.174>.
 70. A. Jain, and A.K. Panwar, Synergetic Effect of Rare-Earths Doping on the Microstructural and Electrical properties of Sr and Ca Co-doped BaTiO₃ Nanoparticles. *Ceram. Int.* 46, 10270 (2020). <https://doi.org/10.1016/j.ceramint.2020.01.020>.
 71. J. Sharma, N. Sharma, J. Parashar, V.K. Saxena, D. Bhatnagar, and K.B. Sharma, Dielectric Properties of Nanocrystalline Co-Mg Ferrites. *J. Alloys Compd.* 649, 362 (2015). <https://doi.org/10.1016/j.jallcom.2015.07.103>.

Publisher's Note Springer Nature remains neutral with regard to jurisdictional claims in published maps and institutional affiliations.